



A metamaterial beam with inverse nonlinearity for broadband micro-vibration attenuation

Xiaodong Zhang^{a,b}, Huiyong Yu^a, Zhicheng He^a, Guoliang Huang^b, Yangyang Chen^{b,*}, Gang Wang^{a,*}

^a State Key Laboratory of Advanced Design and Manufacturing for Vehicle Body, Hunan University, 410082 Changsha, China

^b Department of Mechanical and Aerospace Engineering, University of Missouri, Columbia, MO 65211, USA

ARTICLE INFO

Article history:

Received 9 October 2020

Received in revised form 27 January 2021

Accepted 4 March 2021

Available online xxxx

Keywords:

Metamaterial

Piezoelectric shunting

Nonlinear effect

Micro-vibration

Digital controller

Inverse nonlinearity

ABSTRACT

Strong nonlinearity usually becomes noticeable when nonlinear materials or structures undergo large deformation. However, we present here the inverse nonlinearity, where the nonlinearity is inversely proportional to the deformation. We demonstrate this peculiar behavior in a nonlinear metamaterial beam, which is endowed with an array of piezoelectric patches shunted with nonlinear digital oscillators. The nonlinear digital oscillator is physically suggested by coding digital controllers to form an effective nonlinear capacitor, which is connected to an analog inductor. We also analytically interpret this inverse nonlinearity through the effective bending stiffness of the metamaterial beam. It is found that the vibration attenuation bandwidth of the nonlinear metamaterial beam under small-amplitude excitations is three times larger than that under relatively large-amplitude excitations. Thanks to the programmability of digital circuits, the nonlinear oscillators can be easily tuned with various nonlinearities, making vibration control adaptable in both penetration strength and frequency bands. The nonlinear metamaterial beam enlarges vibration control in both frequency and amplitude domains and sheds lights on broadband low-intensity sound and micro-vibration control.

© 2021 Elsevier Ltd. All rights reserved.

1. Introduction

Nonlinear springs that display a nonlinear relationship between force and displacement are fundamental elements in nonlinear mechanical structures and systems. This nonlinear relationship can be approximately described by a polynomial function with order n greater than 1 to characterize nonlinearity. In general, for naturally occurring materials, $n = 3$ is the most popular choice, which provides good approximations on force and displacement relations when the spring experiences large deformation. In this situation, the relation between force and displacement increasingly diverges from its linear relation when the deformation becomes larger. As a result, the spring can be considered as a linear spring if the deformation is sufficiently small, and nonlinearity arises only for relatively large deformation. In other words, “Nonlinearity” is proportional to deformation. On the other hand, there exists, at least mathematically, another choice of nonlinear characterization, i.e. $n = 1/3$. For this choice, the nonlinear relation between force and displacement increasingly converges to the linear relation when the deformation becomes larger. “Nonlinearity” only arises for sufficiently small deformation and is inversely propor-

* Corresponding authors.

E-mail addresses: xzd_zhang@hnu.edu.cn (X. Zhang), yc896@missouri.edu (Y. Chen), wangg@hnu.edu.cn (G. Wang).

tional to the deformation. In this study, we call such behavior “inverse nonlinearity”. However, inverse nonlinearity has obtained little or no attention, largely because existing materials developed to date usually cannot display this property.

Mechanical metamaterials, artificial composites[1,2], exhibit unusual mechanical properties not appeared in nature, i.e. negative mass density, negative modulus, or negative Poisson’s ratio, et al. Mechanical metamaterials have enabled a range of promising applications included but not limited in acoustic/elastic wave suppression and attenuation[3–11], negative refraction[12–14], topological insulators[15–17], and cloaking[18–20]. Introducing a nonlinear degree of freedom into metamaterial designs has recently been proved as an appealing solution for achieving broadband low-frequency wave/vibration mitigation[21–23]. When waves passing through nonlinear acoustic metamaterials, bifurcations[24–26], chaotic bands [27,28], and amplitude-dependent bandgaps[29,30] can arise. In previous studies, nonlinearities considered in mechanical metamaterials are proportional to deformation. How to design a mechanical metamaterial that can display inverse nonlinearity, and how inverse nonlinearity provides striking engineering solutions in wave and vibration control have never been explored before.

Here, inspired by the piezoelectric shunt technique[31–39], we design a nonlinear metamaterial beam attached by an array of piezoelectric patches that are shunted with nonlinear digital oscillators. The nonlinear digital oscillator contains a linear inductor and a nonlinear capacitor connected in parallel. The nonlinear capacitor manifests an inverse nonlinear relationship between the charge and voltage in the electrical domain, which in turn enables an inverse nonlinear relationship between the stress and strain in the mechanical domain of the metamaterial through the electromechanical coupling. The metamaterial, therefore, exhibits inverse nonlinearity. We show analytically, numerically, and experimentally that the vibration attenuation bandwidth of the nonlinear metamaterial under small-amplitude excitations is three times large than that with relatively large-amplitude excitations, due to the inverse nonlinearity. The proposed nonlinear metamaterial provides a new way in tailoring of mechanical nonlinearity, i.e. through digital electrical circuits. Potential applications may include broadband micro-vibration suppression for spacecraft or precise instruments.

2. Design of a metamaterial beam with inverse nonlinearity

Fig. 1 shows the schematic of a metamaterial beam with inverse nonlinearity. To construct the metamaterial, an array of piezoelectric (lead zirconate titanate, PZT) patches are bonded on one side of the host beam. Each of the patches is shunted with a nonlinear digital oscillator composed of a nonlinear capacitor and a linear inductor (Fig. 1a).

2.1. Design and analysis of the nonlinear digital oscillator

In the study, we consider a voltage-controlled nonlinear capacitor for the nonlinear digital oscillator. The relationship between the electric charge q_c and the voltage u_0 of the capacitor is assumed as

$$q_c = \bar{C}_N u_0^{\frac{1}{3}} \quad (1)$$

where \bar{C}_N denotes the nonlinear capacitance. Equation indicates the inverse nonlinearity. Note that this form can be easily realized by a digital control circuit. According to the Kirchhoff’s law, the electrical governing equation of the PZT patch shunted with the nonlinear oscillator with a charge source (see Fig. 2a) reads

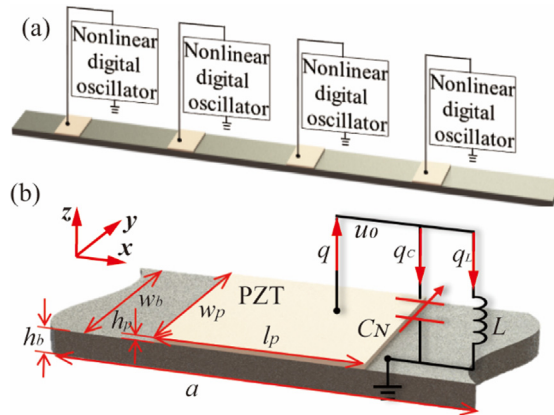


Fig. 1. Design of the nonlinear metamaterial beam: (a) The metamaterial beam with periodic unit cells; (b) Detailed illustration of the metamaterial unit cell.

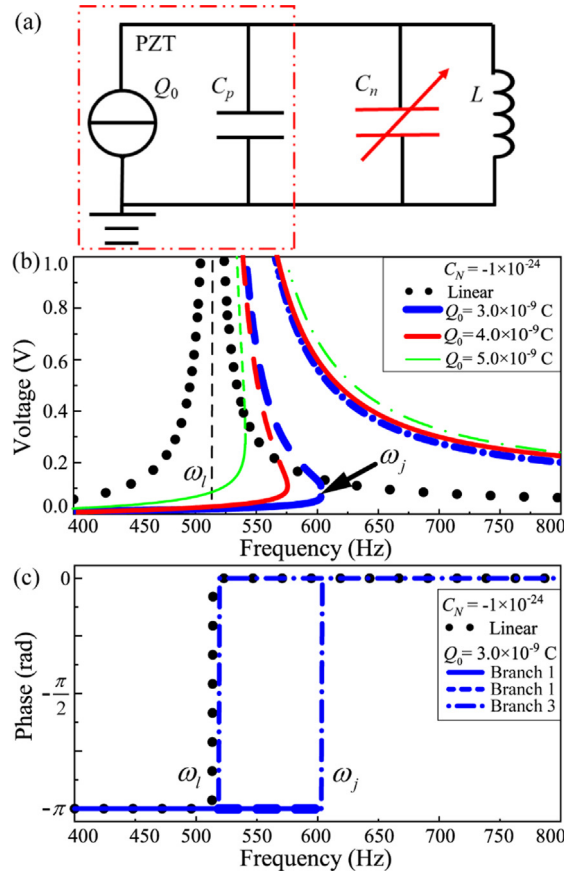


Fig. 2. (a) Representative circuit of a PZT patch shunted with a nonlinear oscillator. (b, c) Frequency responses of the representative circuit excited by a current source: (b) Amplitude; (c) Phase angle.

$$\frac{d^2 Q}{dt^2} = C_p \frac{d^2 u_0}{dt^2} + C_N \frac{d^2 (u_0^{\frac{1}{3}})}{dt^2} + \frac{u_0}{L} \quad (2)$$

where C_p denotes the capacitance of the PZT patch with free boundary conditions, L represents the inductance of the linear inductor, and Q is the charge flowed from the current source. To find frequency responses of the nonlinear electrical circuit, harmonic balance method[40] is applied. We assume the excitation $Q = Q_0 \cos(i\omega t)$, and the solution $u_0 = U_0 \cos(i\omega t)$. At the fundamental order, equation becomes

$$Q_0 = C_p U_0 + \left(\frac{4}{3} C_N U_0 \right)^{\frac{1}{3}} - \frac{U_0}{\omega^2 L} \quad (3)$$

Given Q_0 in equation at different frequencies, frequency responses of U_0 can be obtained.

Fig. 2b and c show the frequency responses of the nonlinear circuit system calculated based on equation. Fig. 2b illustrates the amplitudes of U_0 , and Fig. 2c shows its phase angles. In the calculations, $C_p = 80 \text{ nF}$, $L = 1.2 \text{ H}$, and $C_N = -1 \times 10^{-24} \text{ C}^3 \cdot \text{V}^{-1}$. Frequency responses of the corresponding linear system ($C_N = 0$) are also plotted in Fig. 2b and c for comparison (dotted curves). It can be seen from the figures that, for the linear circuit, unique solutions of frequency responses exist over the entire frequency range. When the excitation frequency reaches to the resonant frequency of the system, the magnitude of the response approaches to infinity, and the phase angle jumps from $-\pi$ to 0. In general, if the excitation, Q_0 , and the response, U_0 , of the electrical circuit are out-of-phase, and, at the same time, the response amplitude is large enough, the metamaterial can attenuate flexural waves or vibrations and generate a band gap at those frequencies through electromechanical coupling[41]. As a consequence, the band gap produced by the linear resonant circuit is usually found at frequencies slightly lower than the resonance frequency of the circuit[42,43]. On the other hand, in the presence of nonlinearity ($C_N = -1 \times 10^{-24} \text{ C}^3 \cdot \text{V}^{-1}$), multiple solutions of frequency responses survive in some frequency regions, dictated by equation. As an illustration, frequency responses with $Q_0 = 3 \times 10^{-9}$, 4×10^{-9} and $5 \times 10^{-9} \text{ C}$ are shown in the figures by three curves with different thicknesses. When $Q_0 = 3 \times 10^{-9} \text{ C}$, three different modes of U_0 are formed at frequencies from 540 to 610 Hz. That is to say when the excitation frequency of Q_0 is within this frequency range, it can generate three possible modes of U_0 at its

excitation frequency. Note that two of the three modes have much stronger responses than the other mode, and the phase angle of one of the two modes is equal to $-\pi$. This indicates the nonlinear metamaterial is capable of attenuating flexural waves or vibrations over this frequency region, which we show in the next section. As can be seen from the figure, the attenuation frequency region due to nonlinearity is much larger than that with the linear circuit, even though it moves slightly to higher frequencies. In addition, by increasing the magnitude of Q_0 to 4×10^{-9} and 5×10^{-9} C, the frequency region where the number of solutions tripled becomes narrower. This phenomenon is in qualitative agreement with the inverse nonlinearity suggested in the study.

2.2. Linearization: Effective bending stiffness and band structure

The effective elastic parameters are necessary for theoretical analysis of band structure as well as the dispersion properties of the metamaterials. The same goes for nonlinear metamaterials, whereas the linearization for nonlinearity is necessary. Despite of the imprecision in linearization of strong nonlinearity, it can still help with qualitative understanding of the dynamic behavior of the nonlinear metamaterials. Therefore, a qualitative study is performed to explore effective elastic parameters of the proposed metamaterial.

Base on the relationship between the q_c and u_0 of the nonlinear capacitor given in equation (1), the effective capacitance can be written as:

$$C_{eff} = \frac{dq_c}{du_0} = \frac{1}{3} \bar{C}_N U_0^{-\frac{2}{3}} \quad (4)$$

where U_0 denotes the amplitude of the excitation voltage. The electrical charge–voltage relation in the frequency domain reads

$$Q_0 = C_{eff} U_0 - \frac{U_0}{\omega^2 L} \quad (5)$$

The constitutive relations of the PZT patch in a beam model can be simplified as [36]

$$\begin{bmatrix} S_1 \\ D_3 \end{bmatrix} = \begin{bmatrix} S_{11}^E & d_{31} \\ d_{31} & \epsilon_{33}^T \end{bmatrix} \begin{bmatrix} T_1 \\ E_3 \end{bmatrix} \quad (6)$$

where S_1 (T_1) denotes the normal strain (stress) along the x -direction, and D_3 and E_3 represent the electric displacement and electric field intensity, respectively. S_{11}^E , ϵ_{33}^T and d_{31} are the compliance coefficients at constant electric field, dielectric constant at constant strain and piezoelectric constant, respectively. The relations between bending curvature $1/\rho$ and strain S_1 can be read

$$\frac{1}{\rho} = \frac{2S_1}{h_b} \quad (7)$$

Combining equations (4) to (7), the linearized effective bending stiffness of the metamaterial beam can be obtained as

$$D_{eff} = \frac{I_p}{S_{11}^E} \left(1 - \frac{\omega^2 d_{31}^2 L A s}{S_{11}^E h_p (1 - \omega^2 L C_p - \frac{1}{3} \omega^2 L C_N U_0^{-\frac{2}{3}})} \right) + E_b I_b \quad (8)$$

The relations between the U_0 and $1/\rho$ can be solved from

$$\left(C_p + \frac{1}{\omega^2 L} \right) U_0 - \frac{\bar{C}_N}{3} U_0^{\frac{1}{3}} + \frac{d_{31} h_b}{2\rho(3^{\frac{2}{3}} S_{11}^E)} = 0 \quad (9)$$

where $I_p = I_p[(h_b + 8h_p)^3 - h_b^3]/24$ and $I_b = I_p h_b^3/24$ are the moment of inertia of the PZT patch (beam) and E_b is the Young's modulus of beam. We can see from equations and that the effective bending stiffness D_{eff} is in function of both the frequency ω and the bending curvature $1/\rho$.

Fig. 3a shows the effective bending stiffness of the nonlinear metamaterial beam at different frequencies with different amplitudes of bending curvatures. Geometric and material parameters of the metamaterial beam are listed in Table 1. In the absence of the nonlinear capacitor (dashed curve), the effective bending stiffness show a resonance behavior, where the effective bending stiffness becomes negative from 491 to 502 Hz. Negative effective bending stiffness usually indicates wave/vibration attenuation in that frequency region[34,35]. In the presence of the nonlinear capacitor, the frequency region of negative effective bending stiffness depends also on the excitation amplitude. For example, when $1/\rho = 5 \times 10^{-10}$, that frequency range is increased and made up a much large region from 571 to 599 Hz. Increasing the amplitude of bending curvature to 2×10^{-9} and 3×10^{-9} , that frequency region is however reduced and narrowed to 526–544 and 508–524 Hz, respectively. Fig. 3b summaries this behavior with more amplitudes of bending curvature calculated. Each vertical line with two short bars on both ends denotes the frequency regions of negative effective bending stiffness. From the figure, we find weak excitations produce broader frequency regions of negative effective bending stiffness, whereas, strong excitations do the

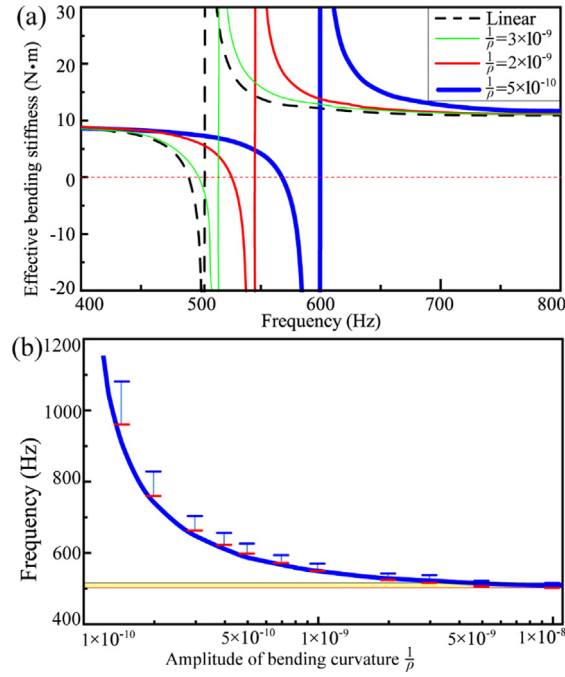


Fig. 3. (a) Linearized frequency-dependent effective bending stiffness of the nonlinear metamaterial beam with different amplitudes of excitation bending curvatures. (b) Frequency regions of negative effective bending stiffness with different amplitudes of excitation bending curvatures.

inverse, making the responses convergent to linear metamaterials. The shown behavior displays inverse nonlinearity. Therefore, the suggested nonlinear metamaterial is particularly useful for low-intensity sound control and micro-vibration attenuation.

2.3. Numerical approach for vibration analysis

To quantify how the resonant shunting circuits with inverse nonlinearity manages the vibration suppression of the metamaterial beam, we develop a numerical approach based on the finite element method. Due to the small width to length and thickness to length ratios of the metamaterial beam, it could be sufficiently accurate by applying Euler–Bernoulli beam assumptions in a one-dimensional setting. According to the standard finite element procedures provided in Ref. [44,45], the discretized piezoelectric-structural coupled equations of motion can be written in terms of nodal displacement and nodal electric potential as

$$\begin{bmatrix} \mathbf{M} & \mathbf{0} \\ \mathbf{0} & \mathbf{0} \end{bmatrix} \begin{bmatrix} \ddot{\mathbf{u}} \\ \ddot{\mathbf{V}} \end{bmatrix} + \begin{bmatrix} \mathbf{K}_u & \mathbf{K}_c \\ \mathbf{K}_c^T & K_v \end{bmatrix} \begin{bmatrix} \mathbf{u} \\ \mathbf{V} \end{bmatrix} = \begin{bmatrix} \mathbf{f} \\ q \end{bmatrix} \quad (10)$$

Table 1

Geometric and material parameters of the aluminum beam and PZT patches.

	Parameter	Symbol	Value
Aluminum beam	Length	l_b	1200 mm
	Width	w_b	40 mm
	Thickness	h_b	3 mm
	Modulus	E_b	69.5 GPa
	Density	ρ_b	2700 kg·m ⁻³
PZT patches	Length	l_p	40 mm
	Width	w_p	40 mm
	Thickness	h_p	0.5 mm
	Density	ρ_p	7600 kg·m ⁻³
	Compliance coefficient	S_{11}^E	$1.8 \times 10^{-12} \text{m}^2 \cdot \text{N}^{-1}$
	Piezoelectric strain constant	d_{31}	$-101 \times 10^{-12} \text{C} \cdot \text{N}^{-1}$
	Dielectric constant	ϵ_{33}^T	$1.8 \times 10^{-8} \text{F} \cdot \text{m}^{-1}$

where \mathbf{u} and V represent the nodal displacement and nodal electric potential of a piezoelectric beam element, \mathbf{f} and q denote the external force applied and free charge flowing into the nodes, respectively. Detailed expressions of the mass, stiffness, piezoelectric capacitance and piezoelectric coupling matrices (\mathbf{M} , \mathbf{K}_u , K_V and \mathbf{K}_c , respectively) can be found in Ref. [45].

The nonlinear electrical shunting circuit controls the electrical boundary condition of the piezoelectric beam, such that the relation between q and V reads

$$\frac{d^2 q}{dt^2} = \frac{V}{L} + C_N^{\frac{1}{3}} \frac{d^2 (V^{\frac{1}{3}})}{dt^2} \quad (11)$$

Taking double derivative with time to the last equation of equation (11), and substituting equation into it, equation (10) becomes

$$\begin{bmatrix} \mathbf{M} & 0 \\ \mathbf{K}_c^T & K_V \end{bmatrix} \begin{bmatrix} \ddot{\mathbf{u}} \\ \ddot{V} \end{bmatrix} + \begin{bmatrix} \mathbf{K}_u & \mathbf{K}_c \\ 0 & -1/L \end{bmatrix} \begin{bmatrix} \mathbf{u} \\ V \end{bmatrix} - \begin{bmatrix} 0 \\ C_N^{\frac{1}{3}} \ddot{V} \end{bmatrix} = \begin{bmatrix} \mathbf{f} \\ 0 \end{bmatrix} \quad (12)$$

where $\ddot{V} = V^{\frac{1}{3}}$. To solve equation (12), we can employ the harmonic balance method (HBM) [46–49] together with the Newton-Raphson method [27,28,50] with given external loadings in a finite nonlinear metamaterial beam.

The HBM is an effective method in solving weak and strong nonlinear problems [40,51–53], and the first order approximation is commonly adopted in almost all cases [22,27,54]. Applying the HBM with the first order approximation (i.e. the first-order HBM), we can firstly assume that the steady response has the form as:

$$\begin{cases} \mathbf{u} = \mathbf{u}_1 \sin(\omega t) + \mathbf{u}_2 \cos(\omega t) \\ V = v_1 \sin(\omega t) + v_2 \cos(\omega t) \\ q_n = a_1 \sin(\omega t) + a_2 \cos(\omega t) \end{cases} \quad (13)$$

where ω is the angular frequency. $\mathbf{u}_{1(2)}$, $v_{1(2)}$ and $a_{1(2)}$ are harmonic components of the nodal displacement \mathbf{u} , nodal electric potential V and the charge of the nonlinear capacitor q_n , respectively. According to equation (1), the components of V can be expressed as: $\begin{cases} v_1 = \frac{3}{4}(a_1^3 + a_1 a_2^2) \\ v_2 = \frac{3}{4}(a_2^3 + a_2 a_1^2) \end{cases} \quad (14)$

Therefore, the first-order HBM leads to the system governed by algebraic equations:

$$\begin{cases} \begin{bmatrix} -\omega^2 \mathbf{M} + \mathbf{K}_u & \mathbf{K}_c \\ -\omega^2 \mathbf{K}_c^T & -\omega^2 K_V - 1/L \end{bmatrix} \begin{bmatrix} \mathbf{u}_1 \\ v_1 \end{bmatrix} + \begin{bmatrix} 0 \\ \omega^2 (\frac{4}{3} C_N)^{\frac{1}{3}} \end{bmatrix} \begin{bmatrix} 0 \\ v_1 (v_1^2 + v_2^2)^{-\frac{1}{3}} \end{bmatrix} = \begin{bmatrix} \mathbf{f} \\ 0 \end{bmatrix} \\ \begin{bmatrix} -\omega^2 \mathbf{M} + \mathbf{K}_u & \mathbf{K}_c \\ -\omega^2 \mathbf{K}_c^T & -\omega^2 K_V - 1/L \end{bmatrix} \begin{bmatrix} \mathbf{u}_2 \\ v_2 \end{bmatrix} + \begin{bmatrix} 0 \\ \omega^2 (\frac{4}{3} C_N)^{\frac{1}{3}} \end{bmatrix} \begin{bmatrix} 0 \\ v_2 (v_1^2 + v_2^2)^{-\frac{1}{3}} \end{bmatrix} = \begin{bmatrix} 0 \\ 0 \end{bmatrix} \end{cases} \quad (15)$$

The solution of equation (15) describes all the responses including $\mathbf{u} = \sqrt{\mathbf{u}_1^2 + \mathbf{u}_2^2}$ under certain excitations \mathbf{f} .

As discussed before, strong nonlinearity may occur when the amplitude of excitation is small. To validate the accuracy of the first-order HBM, we also attempt to increase the harmonic orders to obtain more accurate results. Given that the third harmonic term is usually one of the main harmonic forms for the odd system, the HBM equations with the third-order approximation are also derived here. Similar to the above, assuming that the third-order approximate steady response has the form:

$$\begin{cases} \mathbf{u} = \mathbf{u}_1 \sin(\omega t) + \mathbf{u}_2 \cos(\omega t) + \mathbf{u}_3 \sin(3\omega t) + \mathbf{u}_4 \cos(3\omega t) \\ V = v_1 \sin(\omega t) + v_2 \cos(\omega t) + v_3 \sin(3\omega t) + v_4 \cos(3\omega t) \\ q_n = a_1 \sin(\omega t) + a_2 \cos(\omega t) + a_3 \sin(3\omega t) + a_4 \cos(3\omega t) \end{cases} \quad (16)$$

Thus, V can be expressed as:

$$\begin{cases} v_1 = \frac{3}{4C_N} (a_1^3 + a_1 a_2^2 - a_1^2 a_3 + a_2^2 a_3 + 2a_1 a_3^2 - 2a_1 a_2 a_4 + 2a_1 a_4^2) \\ v_2 = \frac{3}{4C_N} (a_1 a_2^2 + a_2^3 + 2a_1 a_2 a_3 + 2a_2 a_3^2 - a_1^2 a_4 + a_2^2 a_4 + 2a_2 a_4^2) \\ v_3 = \frac{3}{4C_N} (-\frac{1}{3} a_1^3 + a_1 a_2^2 + 2a_1^2 a_3 + 2a_2^2 a_3 + a_3^3 + a_3 a_4^2) \\ v_4 = \frac{3}{4C_N} (\frac{1}{3} a_2^3 - a_1^2 a_2 + 2a_1^2 a_4 + 2a_2^2 a_4 + a_3^3 + a_3^2 a_4) \end{cases} \quad (17)$$

Therefore, the corresponding algebraic equations read:

$$\begin{cases} \begin{bmatrix} -\omega^2 \mathbf{M} + \mathbf{K}_u & \mathbf{K}_c \\ -\omega^2 \mathbf{K}_c^T & -\omega^2 K_V - 1/L \end{bmatrix} \begin{bmatrix} \mathbf{u}_1 \\ v_1 \end{bmatrix} + \begin{bmatrix} 0 \\ \omega^2 a_1 \end{bmatrix} = \begin{bmatrix} \mathbf{f} \\ 0 \end{bmatrix} \\ \begin{bmatrix} -\omega^2 \mathbf{M} + \mathbf{K}_u & \mathbf{K}_c \\ -\omega^2 \mathbf{K}_c^T & -\omega^2 K_V - 1/L \end{bmatrix} \begin{bmatrix} \mathbf{u}_2 \\ v_2 \end{bmatrix} + \begin{bmatrix} 0 \\ \omega^2 a_2 \end{bmatrix} = \begin{bmatrix} 0 \\ 0 \end{bmatrix} \\ \begin{bmatrix} -9\omega^2 \mathbf{M} + \mathbf{K}_u & \mathbf{K}_c \\ -9\omega^2 \mathbf{K}_c^T & -9\omega^2 K_V - 1/L \end{bmatrix} \begin{bmatrix} \mathbf{u}_3 \\ v_3 \end{bmatrix} + \begin{bmatrix} 0 \\ 9\omega^2 a_3 \end{bmatrix} = \begin{bmatrix} 0 \\ 0 \end{bmatrix} \\ \begin{bmatrix} -9\omega^2 \mathbf{M} + \mathbf{K}_u & \mathbf{K}_c \\ -9\omega^2 \mathbf{K}_c^T & -9\omega^2 K_V - 1/L \end{bmatrix} \begin{bmatrix} \mathbf{u}_4 \\ v_4 \end{bmatrix} + \begin{bmatrix} 0 \\ 9\omega^2 a_4 \end{bmatrix} = \begin{bmatrix} 0 \\ 0 \end{bmatrix} \end{cases} \quad (18)$$

By solving the combination of equations (17) and (18), the responses based on the third-order HBM can be obtained.

Fig. 4 illustrates the calculated system responses based on the first-order HBM and the third-order HBM when only one cell in the beam works. As we can see from Fig. 4a, when a small excitation ($F = 0.02$ N) is applied to the metamaterial beam, the vibration suppression band in the first-order HBM case locates from 493 Hz to 522 Hz, while that corresponding the third-order HBM case is almost the same (from 494 Hz to 521 Hz). While the amplitude of excitation is increased (e.g. to 0.5 N), good matching can always be found between both results calculated with the first-order and the third-order HBM. More generally, Fig. 4b validates the first-order and the third-order HBMs by comparing the calculated upper and lower boundaries of the attenuation frequency regions with different excitations. It can be seen that the results coincide well. Different from the normal nonlinear case, stronger nonlinearity occurs with smaller excitations. Thus, excitation with amplitude too small will lead to nonlinearity that is too strong, which could cause converge failure and unreasonable results. In our case, good convergence maintains for all excitations with amplitude larger than 0.02 N, while the results calculated with the first-order and the third-order HBM matches well. Thus, to simplify the complexity of calculation, subsequent numerical results will be calculated using only the first-order HBM, and the validity is guaranteed when the excitation is restrained within $F \geq 0.02$ N.

3. Experimental demonstration

To experimentally test vibration responses of the nonlinear metamaterial beam, we fabricate the metamaterial beam with 4 unit cells (Fig. 5a). In experiments, one end of the metamaterial beam is fixed to an electromagnetic shaker and the other

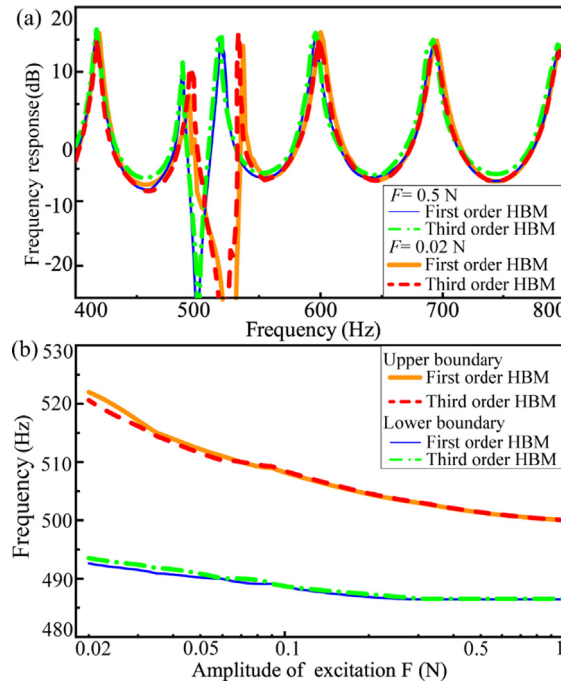


Fig. 4. (a) The frequency responses considering the first-order and the third-order harmonic with excitations $F = 0.5$ N and 0.02 N. (b) The upper and lower boundary frequencies of vibration suppression of the nonlinear metamaterial beam with different amplitudes of excitations, which are calculated based on the first-order and the third-order HBM respectively.

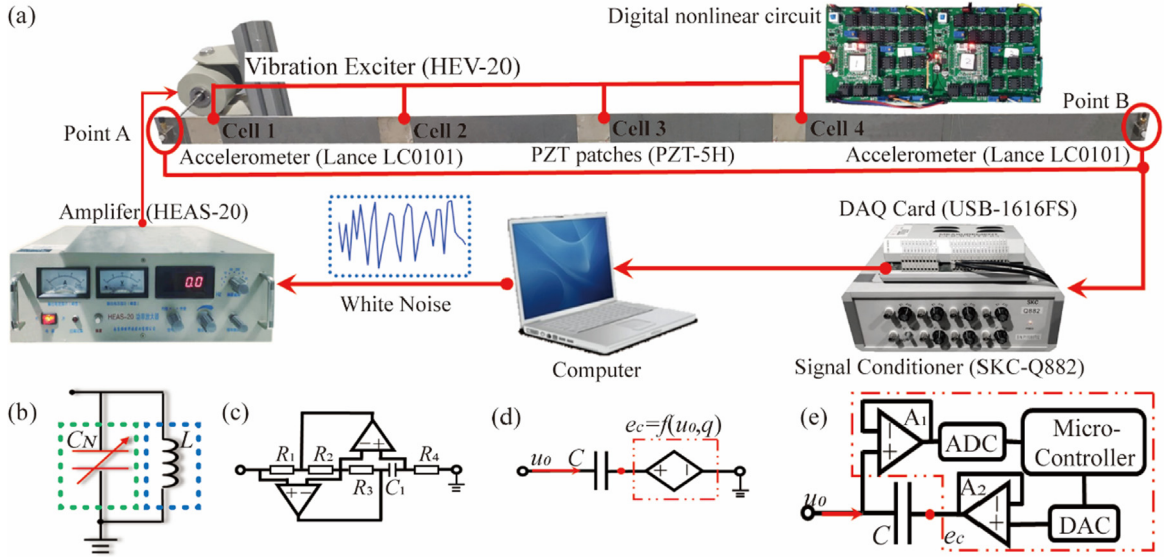


Fig. 5. (a) Experimental setup of vibration tests of the nonlinear metamaterial beam. (b) High-level schematic of the nonlinear oscillator. (c) Circuit diagram of the analog inductor. (d) Illustration of the realization of the nonlinear capacitor with a controlled voltage source. (e) Circuit diagram of the nonlinear capacitor realized by a digital controller.

end is left free. Two accelerometers are attached on both ends of the metamaterial beam to measure its frequency responses. All the geometric and material parameters used in experiments are the same as those in the simulations listed in Table 1.

The nonlinear oscillator consists of a nonlinear capacitor and a linear inductor connected in parallel (Fig. 5b). The linear inductor is designed by a synthetic analog circuits (Fig. 5c) [35]. The nonlinear capacitor is realized by a digital controller. The mechanism can be understood from Fig. 5d. Consider the digital controller as a voltage source, e_c , which is connected to a reference capacitor, C . The relationship between input voltage, u_0 and the output voltage, e_c reads

$$u_0 = \frac{q_c}{C} + e_c \quad (19)$$

Combining equations (1) and (19), we have

$$e_c = u_0 - \frac{\bar{C}_N \cdot u_0^{\frac{1}{3}}}{C} \quad (20)$$

Digital controller can be easily tuned in order to generate various dynamic characteristics by programming [34]. Nonlinearity, as one interesting behavior, can also be realized by them. To implement the relation indicated by equation (20), we design and implement a digital control unit. It consists of an input amplifier A1 (OP07CP), a microcontroller (STM32F446) with embedded ADCs and DACs, and an output amplifier A2 (OP07CP) (see Fig. 5e). In particular, the input amplifier A1 is employed to measure the voltage u_0 . The measured analog voltage signal is digitalized by the ADC, and then fed to the microcontroller for real-time computation. The DAC converts the output digital signal from the microcontroller to an analog signal and pass it to the output amplifier A2. The amplifier A2 applies the voltage e_c to the reference capacitor and the digital control unit effectively functions as the nonlinear capacitor after coding the microcontroller according to equation (20). Detailed parameters of the analog and digital circuits are given in Table 2. The charge–voltage relation of the nonlinear capacitor is tested using MATLAB Simulink (Fig. 6). The solid curve in Fig. 6 represents the result calculated with the time-domain sim-

Table 2
Circuitual parameters of the nonlinear oscillator.

	Symbol	Value
Inductor	R_1	10 K Ω
	R_2	0 ~ 100 K Ω
	R_3	10 K Ω
	R_4	10 K Ω
	C_1	33 nF
Digital capacitor	C	18 nF

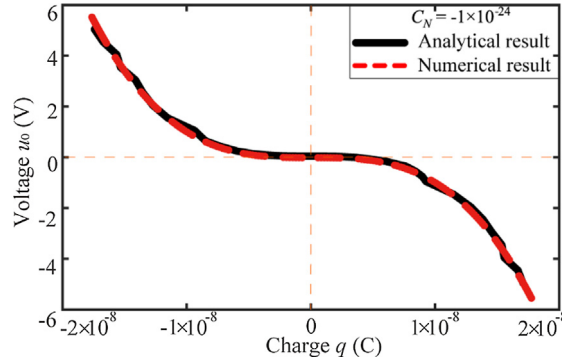


Fig. 6. Charge-voltage relationship of the digital nonlinear capacitor calculated based on analytical and numerical approaches.

ulations based on MATLAB Simulink, while the dashed curve is plotted according to equation (20). In the study, $C_N = -1 \times 10^{-24} \text{ C}^3 \cdot \text{V}^{-1}$. It can be clearly seen that the two results have very good agreement and demonstrate the inverse nonlinearity. The proposed digital controller is ready to be implemented into the nonlinear metamaterial beam for vibration tests.

There are also practical limitations about the nonlinear metamaterial beam in experiments. On the one hand, there always exist electromagnetic interference caused by other electronic devices and background noise, so the voltage measured by ADC can be a few millivolts even without excitation. Moreover, the resolution of ADC and DAC cannot be infinitely small (e.g. no less than 0.8 mV in our instruments). Taking these factors into consideration, the excitation power should not be lesser than 1 W to ensure that the measured voltage amplitude from ADC cannot be lower than 10 mV.

On the other hand, the value of the negative effective capacitance should not be too close or larger than the inherent capacitances of PZT patches in order to avoid any instability of the whole system. According to equation (20), the value of the effective capacitance is thus restrained to be larger than -70 nF in our experiment.

Fig. 7 shows the frequency responses of the nonlinear metamaterial beam with different excitation amplitudes. In all the sub-figures of Fig. 7, the dashed and thick solid curves are from experimental measurements, and the other two curves are from numerical simulations. In experiments, we apply white noise excitations to the point “A” of the beam through an electromagnetic shaker, and measure frequency responses from the point “B” on the beam using an accelerometer. Numerical simulations are performed based on the same setup and calibrated with experiments. Note that in numerical simulations we use the same force excitation over the entire frequency region, which has shown reasonable agreement with experimental measurements. For comparisons, frequency responses of the metamaterial beam with linear resonant circuits are plotted in Fig. 7c. As shown in this figure, the second resonance peak of the metamaterial beam without the circuits can be effectively attenuated producing a clear dip at frequencies from 470 to 520 Hz. Good agreement between numerical and experimental results is clearly seen. By enabling nonlinear capacitors in the resonance circuits, the metamaterial beam displays nonlinearity. In Fig. 7a, we apply a small excitation to the metamaterial beam with the output power from the amplifier being around 2 W among all frequencies and left other circuit parameters the same as those in Fig. 7. We find the vibration attenuation frequency region is enlarged occupying frequencies from 470 to 650 Hz, almost three times wider than the linear case. By increasing the excitation power of the amplifier to almost 20 W, the wave attenuation frequency region shrinks to almost the linear case, demonstrating inverse nonlinearity. Good agreement between numerical and experimental results of the nonlinear metamaterial beam is clearly seen again.

To clearly show how the vibration suppression frequency region changes with different excitation amplitudes of the metamaterial with inverse nonlinearity, Fig. 8 plots numerically calculated frequency regions with tens of different excitations. In this paper, the frequency region of vibration suppression is defined as: within which the frequency response of vibration is below 0 dB. In Fig. 8, the vibration suppression frequency region of the proposed metamaterial with the inverse nonlinearity is represented as the vertical lines (with 2 short bar on both ends for each vertical line), while the region corresponding to the linear case (when the nonlinear capacitor is absent) is marked as the shaded region. As shown in the figure, when decreasing amplitudes of excitations, the vibration attenuation frequency region moves to higher frequencies and occupies much broader frequency regions. When the amplitude of excitations is greater than 0.1 N, the nonlinear metamaterial behaves as a linear metamaterial. All these phenomena once again indicate the inverse nonlinearity of metamaterial beam developed in this study.

The vibration attenuation frequency region can also be flexibly tuned by implementing different circuit parameters. For example, in Fig. 9, we select L as 0.95H. The wave vibration attenuation frequency regions are tuned to 575–720 Hz and 575–600 Hz with the excitation power being about 2 W and 20 W, respectively.

4. Conclusion

In the study, we design a nonlinear metamaterial beam with inverse nonlinearity that has never been explored before. In the design, we mount an array of piezoelectric patches on a beam and shunt them with nonlinear digital oscillators. In par-

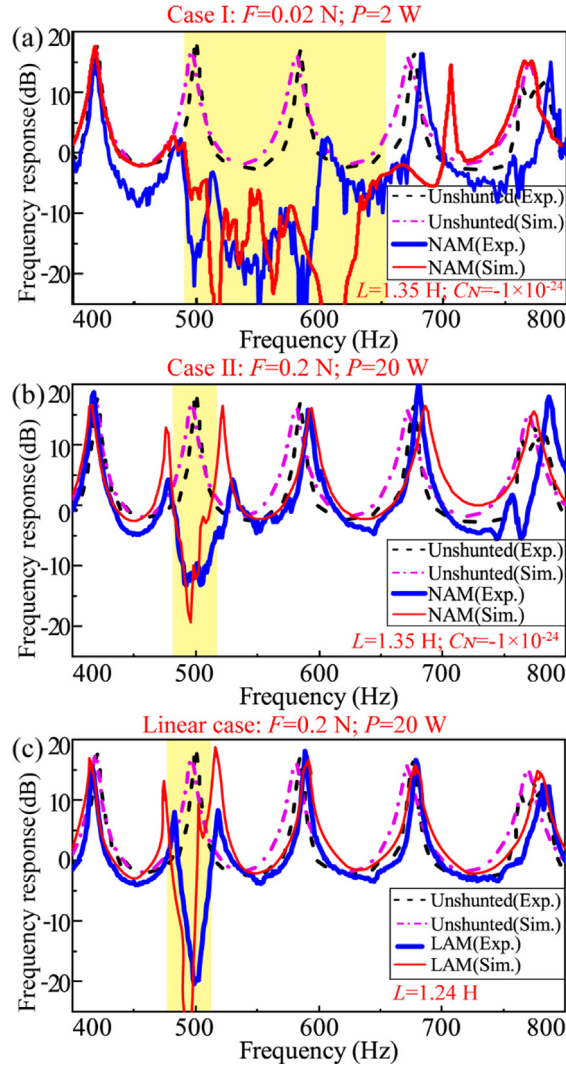


Fig. 7. (a, b) Frequency responses of the nonlinear metamaterial beam from experimental measurements and numerical simulations with different excitations: (a) $P = 2$ W; (b) $P = 20$ W. (c) Frequency responses of the linear metamaterial beam from experimental measurements and numerical simulations.

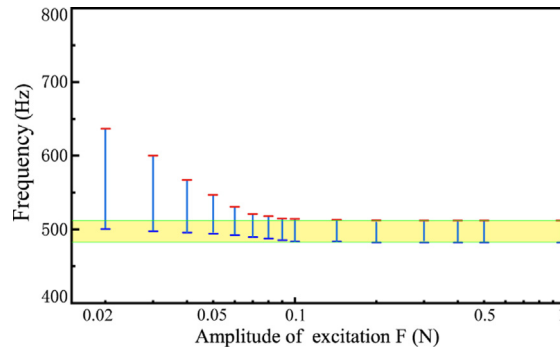


Fig. 8. Frequency regions of vibration suppression of the nonlinear metamaterial beam with different amplitudes of excitations.

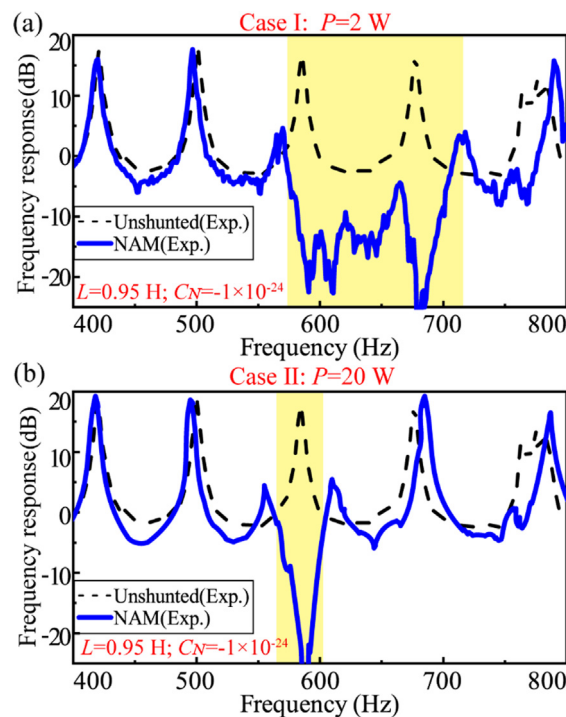


Fig. 9. Experimentally measured frequency responses of the detuned nonlinear metamaterial beam with $L = 0.95H$: (a) $P = 2$ W; (b) $P = 20$ W.

tical, the nonlinear digital oscillator allows an inverse nonlinear relationship between the stress and strain of the metamaterial. Through analytically, numerically, and experimentally studies, we show the negative stiffness and the vibration attenuation bandwidth of the nonlinear metamaterial under small-amplitude excitations is larger than that with relatively large-amplitude excitations, thanks to the inverse nonlinearity. Effective material parameters of the metamaterial and the wave attenuation region can be easily and flexibly tuned by coding the microcontrollers, making the metamaterial able to adapt with excitations.

CRediT authorship contribution statement

Xiaodong Zhang: Conceptualization, Methodology, Software, Investigation, Writing - original draft. **Huiyong Yu:** Investigation, Validation, Formal analysis. **Zhicheng He:** Writing - review & editing. **Guoliang Huang:** Writing - review & editing, Funding acquisition. **Yangyang Chen:** Writing - review & editing, Supervision. **Gang Wang:** Resources, Writing - review & editing, Supervision, Funding acquisition, Project administration.

Declaration of Competing Interest

The authors declare that they have no known competing financial interests or personal relationships that could have appeared to influence the work reported in this paper.

Acknowledgements

This work was supported by the National Natural Science Foundation of China (Grant Nos. 11772123) and Hunan Provincial Innovation Foundation for Postgraduate. The first author, Xiaodong Zhang, would like to thank the support from the China Scholarship Council (CSC). G. Huang acknowledges the Air Force Office of Scientific Research under Grant No. AF AF9550-20-1-0279 with Program Manager Dr. Byung-Lip (Les) Lee.

References

- [1] G. Ma, P. Sheng, Acoustic metamaterials: from local resonances to broad horizons, *Sci. Adv.* 2 (2016) e1501595.
- [2] S. Zhu, X. Zhang, Metamaterials: artificial materials beyond nature, *Natl. Sci. Rev.* 5 (2018) 131.
- [3] M.V. Barnhart, X. Xu, Y. Chen, S. Zhang, J. Song, G. Huang, Experimental demonstration of a dissipative multi-resonator metamaterial for broadband elastic wave attenuation, *J. Sound Vib.* 438 (2019) 1–12, <https://doi.org/10.1016/j.jsv.2018.08.035>.

- [4] X. Zhang, H. Zhang, Z. Chen, G. Wang, Simultaneous realization of large sound insulation and efficient energy harvesting with acoustic metamaterial, *Smart Mater. Struct.* 27 (2018) 105018.
- [5] X. Zhang, Z. He, G. Wang, Extraordinary sound transmission through geometrical mismatched channels based on near zero bulk modulus and Fabry-Pérot resonance, *J. Phys. Appl. Phys.* 52 (2019) 055301.
- [6] K. Yu, N.X. Fang, G. Huang, Q. Wang, Magnetoactive acoustic metamaterials, *Adv. Mater.* 30 (2018) 1706348.
- [7] Z. Tian, C. Shen, J. Li, E. Reit, Y. Gu, H. Fu, S.A. Cummer, T.J. Huang, Programmable acoustic metasurfaces, *Adv. Funct. Mater.* 29 (13) (2019) 1808489, <https://doi.org/10.1002/adfm.201808489>.
- [8] G. Hu, A.C.M. Austin, V. Sorokin, L. Tang, Metamaterial beam with graded local resonators for broadband vibration suppression, *Mech. Syst. Signal Process.* 146 (2021) 106982.
- [9] G. Hu, L. Tang, X. Cui, On the modelling of membrane-coupled Helmholtz resonator and its application in acoustic metamaterial system, *Mech. Syst. Sig. Process.* 132 (2019) 595–608, <https://doi.org/10.1016/j.ymssp.2019.07.017>.
- [10] J. Jung, H.-G. Kim, S. Goo, K.-J. Chang, S. Wang, Realisation of a locally resonant metamaterial on the automobile panel structure to reduce noise radiation, *Mech. Syst. Sig. Process.* 122 (2019) 206–231, <https://doi.org/10.1016/j.ymssp.2018.11.050>.
- [11] Z. Liu, R. Rumlper, L. Feng, Locally resonant metamaterial curved double wall to improve sound insulation at the ring frequency and mass-spring-mass resonance, *Mech. Syst. Signal Process.* 149 (2021) 107179.
- [12] Z. Hou, H. Ni, B. Assouar, PT-symmetry for elastic negative refraction, *Phys. Rev. Appl.* 10 (2018) 044071.
- [13] S. Tong, C. Ren, W. Tang, High-transmission negative refraction in the gradient space-coiling metamaterials, *Appl. Phys. Lett.* 114 (2019) 204101.
- [14] Z. Cai, S. Zhao, Z. Huang, Z. Li, M. Su, Z. Zhang, Z. Zhao, X. Hu, Y.-S. Wang, Y. Song, Bubble architectures for locally resonant acoustic metamaterials, *Adv. Funct. Mater.* 29 (2019) 1906984.
- [15] R. Fleury, A.B. Khanikaev, A. Alu, Floquet topological insulators for sound, *Nat. Commun.* 7 (2016) 11744.
- [16] X. Liu, Q. Guo, J. Yang, Miniaturization of Floquet topological insulators for airborne acoustics by thermal control, *Appl. Phys. Lett.* 114 (2019) 054102.
- [17] Y. Liu, X. Chen, Y. Xu, Topological phononics: from fundamental models to real materials, *Adv. Funct. Mater.* 30 (2020) 1904784.
- [18] H. Nassar, Y.Y. Chen, G.L. Huang, Polar metamaterials: a new outlook on resonance for cloaking applications, *Phys. Rev. Lett.* 124 (2020) 084301.
- [19] H. Nassar, Y.Y. Chen, G.L. Huang, Isotropic polar solids for conformal transformation elasticity and cloaking, *J. Mech. Phys. Solids* 129 (2019) 229–243, <https://doi.org/10.1016/j.jmps.2019.05.002>.
- [20] X. Xu, C. Wang, W. Shou, Z. Du, Y. Chen, B. Li, W. Matusik, N. Hussein, G. Huang, Physical realization of elastic cloaking with a polar material, *Phys. Rev. Lett.* 124 (2020) 114301.
- [21] Z. Lu, Z. Wang, Y. Zhou, X. Lu, Nonlinear dissipative devices in structural vibration control: a review, *J. Sound Vib.* 423 (2018) 18–49, <https://doi.org/10.1016/j.jsv.2018.02.052>.
- [22] X. Fang, J. Wen, D. Yu, J. Yin, Bridging-coupling band gaps in nonlinear acoustic metamaterials, *Phys. Rev. Appl.* 10 (2018) 054049.
- [23] A. Javidiaesaadi, N.E. Wierschem, An inerter-enhanced nonlinear energy sink, *Mech. Syst. Sig. Process.* 129 (2019) 449–454, <https://doi.org/10.1016/j.ymssp.2019.04.047>.
- [24] E. Medina, P.E. Farrell, K. Bertoldi, C.H. Rycroft, Navigating the landscape of nonlinear mechanical metamaterials for advanced programmability, *Phys. Rev. B* 101 (2020) 064101.
- [25] A. Gillman, K. Fuchi, P.R. Buskohl, Truss-based nonlinear mechanical analysis for origami structures exhibiting bifurcation and limit point instabilities, *Int. J. Solids Struct.* 147 (2018) 80–93, <https://doi.org/10.1016/j.ijsolstr.2018.05.011>.
- [26] M. Bukhari, O. Barry, Spectro-spatial analyses of a nonlinear metamaterial with multiple nonlinear local resonators, *Nonlinear Dyn* 99 (2) (2020) 1539–1560, <https://doi.org/10.1007/s11071-019-05373-z>.
- [27] X. Fang, J. Wen, B. Bonello, J. Yin, D. Yu, Ultra-low and ultra-broad-band nonlinear acoustic metamaterials, *Nat. Commun.* 8 (2017) 1288.
- [28] X. Fang, J. Wen, B. Bonello, J. Yin, D. Yu, Wave propagation in one-dimensional nonlinear acoustic metamaterials, *New J. Phys.* 19 (2017) 053007.
- [29] J.M. Manimala, C.T. Sun, Numerical investigation of amplitude-dependent dynamic response in acoustic metamaterials with nonlinear oscillators, *J. Acoustical Soc. Am.* 139 (6) (2016) 3365–3372, <https://doi.org/10.1121/1.4949543>.
- [30] W. Jiao, S. Gonella, Intermodal and subwavelength energy trapping in nonlinear metamaterial waveguides, *Phys. Rev. Appl.* 10 (2018) 024006.
- [31] Y. Chen, X. Li, H. Nassar, G. Hu, G. Huang, A programmable metasurface for real time control of broadband elastic rays, *Smart Mater. Struct.* 27 (2018) 115011.
- [32] X. Li, Y. Chen, G. Hu, G. Huang, A self-adaptive metamaterial beam with digitally controlled resonators for subwavelength broadband flexural wave attenuation, *Smart Mater. Struct.* 27 (2018) 045015.
- [33] K. Yi, G. Matten, M. Ouisse, E. Sadoulet-Reboul, M. Collet, G. Chevallier, Programmable metamaterials with digital synthetic impedance circuits for vibration control, *Smart Mater. Struct.* 29 (3) (2020) 035005, <https://doi.org/10.1088/1361-665X/ab6693>.
- [34] G. Wang, J. Cheng, J. Chen, Multi-resonant piezoelectric shunting induced by digital controllers for subwavelength elastic wave attenuation in smart metamaterial, *Smart Mater. Struct.* 26 (2017) 025031.
- [35] X. Zhang, F. Chen, Z. Chen, G. Wang, Membrane-type smart metamaterials for multi-modal sound insulation, *J. Acoust. Soc. Am.* 144 (6) (2018) 3514–3524, <https://doi.org/10.1121/1.5084039>.
- [36] G. Wang, S. Chen, Large low-frequency vibration attenuation induced by arrays of piezoelectric patches shunted with amplifier-resonator feedback circuits, *Smart Mater. Struct.* 25 (2016) 015004.
- [37] C. Lan, W. Qin, Enhancing ability of harvesting energy from random vibration by decreasing the potential barrier of bistable harvester, *Mech. Syst. Sig. Process.* 85 (2017) 71–81, <https://doi.org/10.1016/j.ymssp.2016.07.047>.
- [38] P. Gardonio, M. Zientek, L. Dal Bo, Panel with self-tuning shunted piezoelectric patches for broadband flexural vibration control, *Mech. Syst. Signal Process.* 134 (2019) 106299.
- [39] L. Sirota, F. Semperlotti, A.M. Annaswamy, Tunable and reconfigurable mechanical transmission-line metamaterials via direct active feedback control, *Mech. Syst. Sig. Process.* 123 (2019) 117–130, <https://doi.org/10.1016/j.ymssp.2019.01.001>.
- [40] J. Lu, X. Zhao, S. Yamada, *Harmonic Balance Finite Element Method: Applications in Nonlinear Electromagnetics and Power Systems*, first ed., John Wiley & Sons Inc, New York, 2016.
- [41] M. Berardengo, J. Hogsberg, S. Manzoni, M. Vanali, A. Brandt, T. Godi, LRLC-shunted piezoelectric vibration absorber, *J. Sound Vib.* 474 (2020) 115268.
- [42] F. Casadei, M. Ruzzene, L. Dozio, K.A. Cunefare, Broadband vibration control through periodic arrays of resonant shunts: experimental investigation on plates, *Smart Mater. Struct.* 19 (1) (2010) 015002, <https://doi.org/10.1088/0964-1726/19/1/015002>.
- [43] L. Airoldi, M. Ruzzene, Design of tunable acoustic metamaterials through periodic arrays of resonant shunted piezos, *New J. Phys.* 13 (2011) 113010.
- [44] S.S. Rao, *The Finite Element Method in Engineering*, Butterworth-Heinemann, 2017.
- [45] H. Allik, T.J.R. Hughes, Finite element method for piezoelectric vibration, *Int. J. Numer. Meth. Engng.* 2 (2) (1970) 151–157, <https://doi.org/10.1002/nme.1620020202>.
- [46] M. Jahn, S. Tatzko, L. Panning-von Scheidt, J. Wallaschek, Comparison of different harmonic balance based methodologies for computation of nonlinear modes of non-conservative mechanical systems, *Mech. Syst. Sig. Process.* 127 (2019) 159–171, <https://doi.org/10.1016/j.ymssp.2019.03.005>.
- [47] X.-Y. Mao, J.-Q. Sun, H. Ding, L.-Q. Chen, An approximate method for one-dimensional structures with strong nonlinear and nonhomogeneous boundary conditions, *J. Sound Vib.* 469 (2020) 115128.
- [48] T.-C. Yuan, J. Yang, L.-Q. Chen, A harmonic balance approach with alternating frequency/time domain progress for piezoelectric mechanical systems, *Mech. Syst. Sig. Process.* 120 (2019) 274–289, <https://doi.org/10.1016/j.ymssp.2018.10.022>.
- [49] A. Beléndez, A. Hernández, T. Beléndez, M.L. Álvarez, S. Gallego, M. Ortuño, C. Neipp, Application of the harmonic balance method to a nonlinear oscillator typified by a mass attached to a stretched wire, *J. Sound Vib.* 302 (4–5) (2007) 1018–1029, <https://doi.org/10.1016/j.jsv.2006.12.011>.

- [50] S.K. Lai, C.W. Lim, B.S. Wu, C. Wang, Q.C. Zeng, X.F. He, Newton–harmonic balancing approach for accurate solutions to nonlinear cubic–quintic Duffing oscillators, *Appl. Math. Model.* 33 (2) (2009) 852–866, <https://doi.org/10.1016/j.apm.2007.12.012>.
- [51] M. Krack, J. Groß, *Harmonic Balance for Nonlinear Vibration Problems*, Springer International Publishing, 2019.
- [52] R.K. Narisetti, M. Ruzzene, M.J. Leamy, Study of wave propagation in strongly nonlinear periodic lattices using a harmonic balance approach, *Wave Motion* 49 (2) (2012) 394–410, <https://doi.org/10.1016/j.wavemoti.2011.12.005>.
- [53] M.S.H. Chowdhury, M.A. Hosen, K. Ahmad, M.Y. Ali, A.F. Ismail, High-order approximate solutions of strongly nonlinear cubic–quintic Duffing oscillator based on the harmonic balance method, *Results Phys.* 7 (2017) 3962–3967, <https://doi.org/10.1016/j.rinp.2017.10.008>.
- [54] P. Shivashankar, S.B. Kandagal, Characterization of elastic and electromechanical nonlinearities in piezoceramic plate actuators from vibrations of a piezoelectric-beam, *Mech. Syst. Sig. Process.* 116 (2019) 624–640, <https://doi.org/10.1016/j.ymssp.2018.06.063>.